Int. J. Electrochem. Sci., 14 **(2019)** 7937 – 7946, doi: 10.20964/2019.08.76

International Journal of
ELECTROCHEMICAL
SCIENCE
www.electrochemsci.org

Sandwich-structured Fe_3O_4/Graphene Hybrid Film for High-Performance Lithium-Ion Batteries

Hua Fang[1,], Fanteng Meng[1], Gaoyun Chen[2], Lixia Wang[1], Shichao Zhang[3,*], Ji Yan[1], Linsen Zhang, Yongxia Zhang[1]*

[1] School of Material and Chemical Engineering, Henan Provincial Key Laboratory of Surface Interface Science, Zhengzhou University of Light Industry, Zhengzhou 450002, PR China
[2] Institute of Chemical Defense, Beijing, 102205, China
[3] School of Materials Science and Engineering, Beihang University, Beijing, 100191, PR China
[*]E-mail: fh@zzuli.edu.cn, csc@buaa.edu.cn

Received: 20 March 2019 / *Accepted:* 10 June 2019 / *Published:* 30 June 2019

Sandwich-structured Fe_3O_4/graphene hybrid film (FGHF) was prepared by electrostatic self-assembly and vacuum filtration. In the constructed architecture, the graphene sheets stacked densely in a nearly face-to-face fashion, while the Fe_3O_4 nanoparticles are homogeneously loaded on graphene nanosheets in a layer-by-layer manner. In this structure, the graphene sheets are supposed to provide high electronic conductivity, accommodate the volume fluctuation of Fe_3O_4, and improve flexibility of the electrode. Moreover, the FGHF exhibited a high surface area and hierarchical pore distribution, which are considered to be beneficial for fast ion transportation, short solid-state diffusion lengths and buffering volume expansion. As expected, the FGHF exhibited high lithium storage capacity (947 mAh g^{-1} at 1 A g^{-1}), excellent rate capability (901, 806, 711 and 598 mAh g^{-1} at 2, 5, 10 and 20 A g^{-1}, respectively) and stable cycle performance (798 mAh g^{-1} after 300 charge-discharge cycles at 1 A g^{-1}).

Keywords: Fe_3O_4, Graphene, Nanocomposites, Lithium-ion batteries, Sandwich structure

1. INTRODUCTION

Lithium-ion batteries (LIBs) are widely used in everyday electrical devices, such as portable electronic devices, electric vehicles and large-scale energy storage [1-3]. Transition metal oxides, such as CuO [4-6], TiO_2 [7, 8], Mn_3O_4 [9, 10], etc., have been extensively studied for next generation LIBs, due to much higher theoretical capacity than graphite. Among them, Fe_3O_4 is a promising anode material for next-generationLIBs due to its superior properties such as storage abundance, high capacity and low cost [11-25]. However, the application of Fe_3O_4 in LIBs is hindered by the severe volume fluctuation during lithiation/delithiation processes, which would trigger electrode pulverization

and rapid capacity fading [26]. Another obstacle is its poor rate performance caused by the low electronic conductivity of Fe_3O_4 [27].

To overcome such obstacles, many researches were focused on fabricating various Fe_3O_4/graphene hybrids, including graphene-wrapped Fe_3O_4 nanostructures [28], Fe_3O_4 nanoparticles anchored on graphene surface [29,30], Fe_3O_4 nanoparticles confined in three-dimensional (3D) graphene network [31,32] and flexible graphene-Fe_3O_4 hybrid films [33,34]. It is generally accepted that graphene nanosheets could provide highly conductive matrix to reduce reaction resistance and buffer high volume changes during cycling [35]. For example, Zhao reported Fe_3O_4/graphene composites by in-situ redox approach. The as-prepared Fe_3O_4/rGO composite delivers a remarkable reversible capacity of 1024 mA h g^{-1} at 1 A g^{-1}, and retains 584 mA h g^{-1} at 5 A g^{-1} even after 450 cycles [29]. Yoon reported an Fe_3O_4/graphene sheets composite, which exhibited a high reversible discharge capacity of 674 mA h g^{-1} at 100 mA g^{-1} [36]. However, achieving high-rate Fe_3O_4 electrodes with long-term cycling stability remains a significant challenge [1].

Herein, a sandwich-structured Fe_3O_4@Graphene hybrid film (FGHF) was constructed by a facile strategy combining electrostatic self-assembly with vacuum filtration. In the constructed architecture, the graphene sheets stacked densely in a nearly face-to-face fashion and Fe_3O_4 nanoparticles (NPs) are homogeneously embedded between these nanosheets in a layer-by-layer manner. Due to the unique sandwich structure, the graphene sheets are supposed to effectively accelerate electron transfer, buffer volume changes of Fe_3O_4, and endow the electrode with flexibility. As expected, a high capacity of 947 mAh g^{-1} was demonstrated at the current density of 1 A g^{-1}, with an excellent cycling stability up to 300 cycles.

2. EXPERIMENTAL

2.1. Materials synthesis

All the chemicals were used in analytical grades without purification. Graphite oxide was synthesized from natural graphite powder by the modified Hummers method [37]. The prepared graphite oxide was ultrasonically dispersed in deionized water to obtain graphene oxide (GO) hydrosol (0.1 g L^{-1}). For preparing $Fe(OH)_3$ colloid solution, 23 mL of urea solution (0.2 M) was added into 100 ml of $FeCl_3$ solution (0.0155 M). Then, the mixed solution was heated up to 80 °C in a water bath and kept at 80 °C for 40 min under magnetic stirring. The obtained the $Fe(OH)_3$ colloid solution was cooled to room temperature for further experiment.

The prepared GO hydrosol was added dropwise into the prepared $Fe(OH)_3$ colloid solution under magnetic stirring. The volume ratio of GO hydrosol and $Fe(OH)_3$ colloid solution was set as 1:2. A flocculent precipitate was formed within a few minutes. Subsequently, $Fe(OH)_3$@GO hybrid film was obtained by vacuum filtration through a microfiltration film. Finally, the $Fe(OH)_3$@GO hybrid film were subjected to heat treatment at 300 ℃ in a tube-furnace under N_2 atmosphere, leading to the formation of FGHF.

2.2. Characterization

The Zeta potentials of $Fe(OH)_3$ colloid solution and GO hydrosol were measured on a particle size and Zeta potential analyzer (Zetaplus). The phases of the samples were examined by using an X-ray diffractometer (XRD, Bruker Axs DS Advance) with Cu Kα radiation, a tube voltage of 40 kV, current of 100 mA and scanning speed of $4°•min^{-1}$.. The morphology of FGHF was studied by field emission scanning electron microscopy (SEM, JSM-7001F) and transmission electron microscope (TEM, JSM-700). The mass content of Fe_3O_4 in FGHF was characterized by thermogravimetric (TG) analysis (in air, 25 mL min^{-1}, 25-900 °C, 10 °C min^{-1}) by using a simultaneous thermal analyzer (Diamond Perkin Elmer S II). Nitrogen adsorption/desorption test was performed at 77K on a specific surface and porosity analyzer (BELSORP-Mini II). The specific surface area was calculated by the conventional Brunauer–Emmett–Teller (BET) method, and the total pore volume was estimated by the amount of N_2 adsorption at a relative pressure of 0.95. The pore size distributions were obtainedby using the nonlocal density functional theory (NLDFT) method.

2.3. Electrochemical measurements

The FGHF electrode was made by pressing the FGHF on nickel foam (1 cm ×1 cm). The CR2032 coin type cells were assembled in a glove box under Ar gas atmosphere, with the FGHF electrode as working electrode, a pure Li foil as counter/reference electrode, 1 M $LiPF_6$ in a 1:1 V/V mixture of ethylene carbonate and diethyl carbonate as an electrolyte, and Cellgard 2400 as separator. Cyclic voltammograms (CV) were tested on an electrochemical workstation (CHI 604) at a scan rate of 0.1 mV s^{-1} (voltage range of 0.01~3.0 V vs Li^+/Li). Galvanostatic charge/discharge (GCD) tests were performed on a battery testing system (Neware CT-4008) between 0.01 V and 3 V (vs Li^+/Li). The GCD current density ranged from 1 to 20.0 A g^{-1}.

To confirm the superiority of the FGHF electrode, bare Fe_3O_4 electrode was also tested by same approach. To obtain bare Fe_3O_4 power, the $Fe(OH)_3$ colloid solution was dried at 80 °C and then subjected to heat treatment at 300 °C in a tube-furnace under N_2 atmosphere. The Fe_3O_4 electrode were prepared by dispersing 80% Fe_3O_4 power, 10% carbon black, 6% sodium carboxymethyl cellulose and 4% SBR dissolved in distilled water and absolute alcohol. Homogeneous slurry was obtained by stirring constantly for 8 h. Finally, the as-prepared slurry was pasted onto copper foil.

3. RESULTS AND DISCUSSION

3.1 Fabrication mechanism

As shown by Fig. 1, the successful fabrication of sandwich-structured FGHF was based on the combination of electrostatic self-assembly and vacuum filtration process. Firstly, The prepared GO hydrosol was added dropwise into the prepared $Fe(OH)_3$ colloid solution under magnetic stirring, during which process $Fe(OH)_3$ colloid nanoparticles are electrostatically self-assembled onto the

surface of GO sheets. Zeta potential was measured to confirm the surface charge of the two collide solutions.

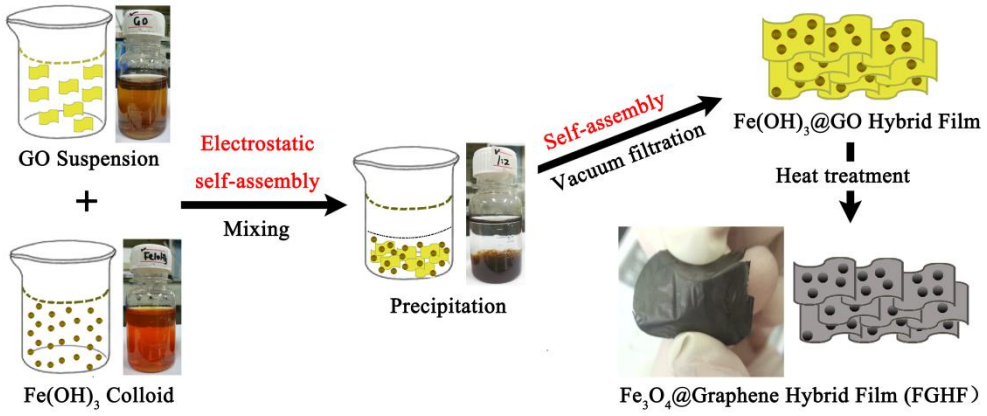

Figure 1. Schematic representation of the fabrication process of the FGHF

The GO colloid showed a negative Zeta potential of -13.5 mV. The $Fe(OH)_3$ colloid, in contrast, showed a positive Zeta potential of 4.2 mV. Then, the produced flocculent precipitate substance is self-assembled into $Fe(OH)_3$@GO hybrid film by vacuum filtration. Finally, the $Fe(OH)_3$@GO hybrid film was subjected to a heat treatment process. In this process, GO sheets was reduced to graphene and the $Fe(OH)_3$ colloid nanoparticles were converted to Fe_3O_4 nanoparticles, resulting in the Sandwich-structured FGHF. As confirmed by the following characterization results, in the constructed architecture, the graphene sheets stacked densely in a nearly face-to-face fashion and Fe_3O_4 nanoparticles (NPs) are homogeneously embedded between these graphene nanosheets in a layer-by-layer manner.

3.2 Materials Characterization

As shown by Fig. 2a and 2b, the FGHF showed a uniform thickness of ~15 μm and a nanoporous sandwich-structured morphology. The graphene sheets stacked densely in a nearly face-to-face fashion and Fe_3O_4 nanoparticles (NPs) are homogeneously embedded between these nanosheets in a layer-by-layer manner. Such morphology should be beneficial for fast ion transportation, short solid-state diffusion lengths and buffering volume expansion/shrinkage during lithiation/delithiation processes. TEM image reveals that Fe_3O_4 NPs with diameter of 10-50 nm are homogeneously anchored on the graphene surface (Fig. 2c). The lattice fringes prove the coexistence of Fe_3O_4 nanoparticles and 2-5 layered graphene (Fig. 2d).

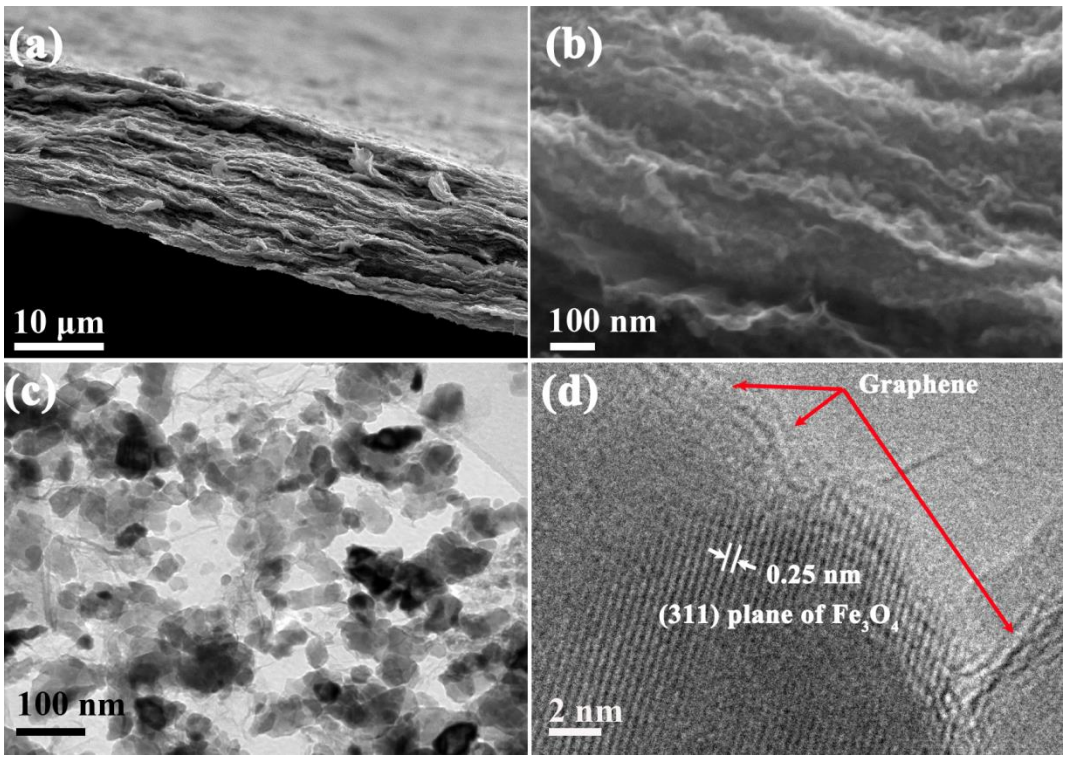

Figure 2. SEM (a, b) and TEM (c, d) images of the FGHF.

As shown in Fig. 3a, the XRD peaks at 12.4°, 17.2°, 27.0°, and 35.7° are in good agreement with (110), (200), (310) and (211) planes of $Fe(OH)_3$ (JCPDS card No. 34-1266). The XRD peaks of 30.2, 35.4, 43.2, 57.3 and 62.9° are well agreed with (220), (311), (400), (511) and (440) crystal planes of face-centered cubic Fe_3O_4 (JCPDS standard card No. 86−1354) [34]. The diffraction peaks are weak for GO and graphene, which may be caused by their low mass content [30]. The TG analysis was performed in air between 25 and 900 °C. The mass percentages of Fe_3O_4 is 82.3 wt% according to the TG curves shown in Fig. 3b.

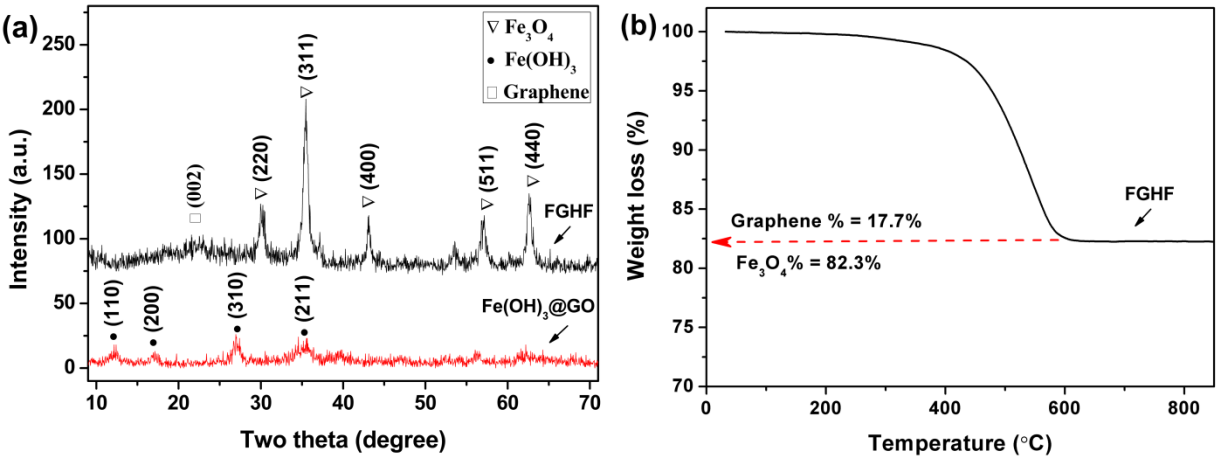

Figure 3. (a) XRD patterns of the $Fe(OH)_3$@GO hybrid film and FGHF, and (b) the TG curve of FGHF.

As shown by Fig. 4a, the FGHF film exhibits typical type-IV N_2 adsorption-desorption isotherms with distinct hysteresis loops within the relative pressure range of 0.45–0.95, indicating the mesoporous structure [38]. The FGHF showed a high surface area of 92.7 m^2 g^{-1}, a total pore volume of 0.3257 cm^3 g^{-1} and an average pore diameter of 27.1 nm. As shown in Fig. 4b, the pore size distribution curve of the FGHF had a wide pore size distribution, indicating the coexistence of mesopores (2-50 nm) and macropores (>50 nm). The high surface area and hierarchical pore distribution are beneficial for fast ion transportation, short solid-state diffusion lengths and buffering volume expansion, which are very important for high-power LIBs [39].

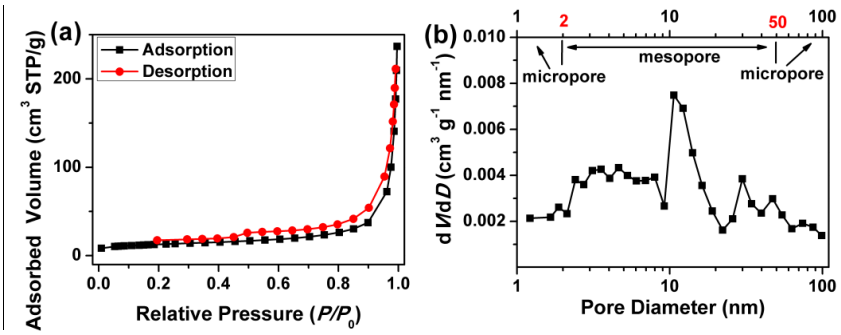

Figure 4. N_2 adsorption isotherms (a) and pore size distributions (b) of the FGHF.

3.3 Electrochemical Characterization

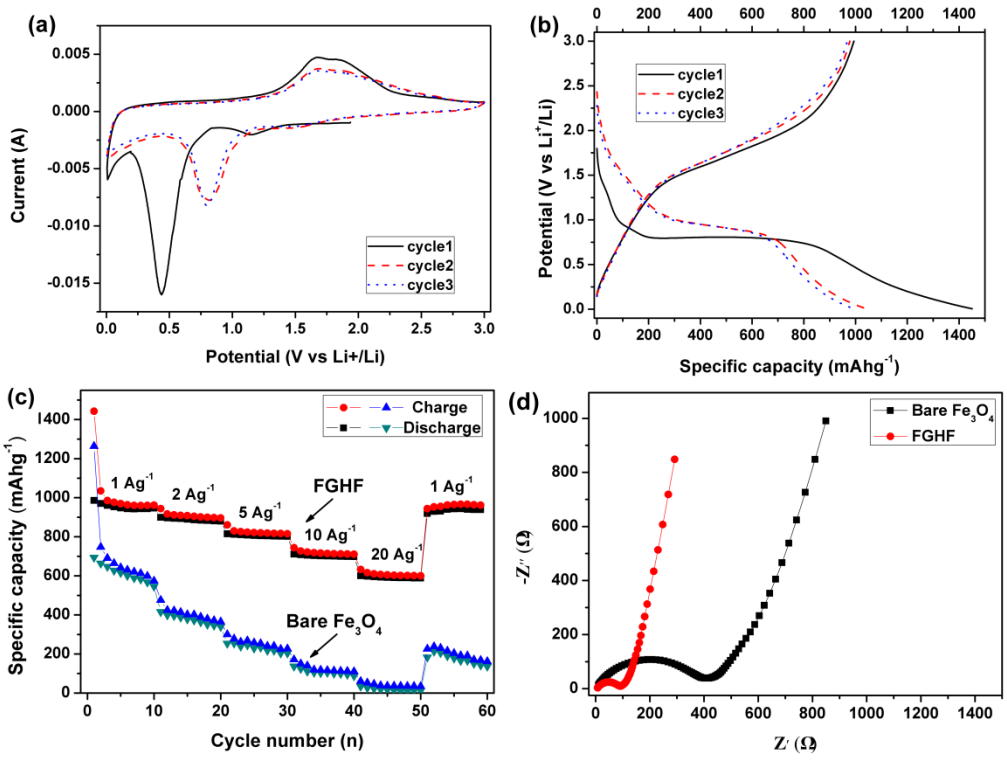

Figure 5. (a) CV curves of the FGHF electrode, (b) GCD curves of the FGHF electrode, (c) rate performances of the FGHF and bare Fe_3O_4 electrode and (d) EIS spectrum of the FGHF and bare Fe_3O_4 electrode.

Then coin cells were assembled to evaluate the superiority of the unique FGHF as anode material of LIBs. The representative CV curves are shown in Fig. 5a. During the first cathodic scan, the peaks at ~1.2 V and ~0.5 V can be corresponding to the Li insertion into Fe_3O_4 and the formation of solid electrolyte interphase (SEI) layer [29, 34]. In the following scans, the peak shifts to 0.8 V with a decreased intensity, which may be caused by some irreversible processes occurred in the first cycle. In the anodic scan, the peaks centered at ~1.8 V can be attributed to the transformation of Fe^{3+} from Fe^0 [34]. The CV curves exhibits little change between the cycle 2 and cycle 3, which indicates the good reversibility of the FGHF.

As shown in Fig. 5b, The first charge capacity of the FGHF reached about 1451 mAh g^{-1} and the first discharge capacity can reach about 994 mAh g^{-1}, corresponding to a coulombic efficiency of about 68.5 %. The coulombic efficiency increased to 93.7 % in the second GCD cycles. Fig. 6 showed cycle performance of the FGHC electrodeat 1 A g^{-1}. The coulombic efficiency increases rapidly and remains close to 99% in the following cycles, indicating its excellent cycle stability.

As expected, the FGHF exhibits an superior high rate capability, as shown in Fig 5(c). The reversible capacity is retained to be 896 mAh g^{-1}, 811 mAh g^{-1},712 mAh g^{-1} and 598 mAh g^{-1} when current density is increased to 2, 5, 10 and 20 A g^{-1}, respectively. When the current rate returns to 1 A g^{-1}, a high capacity of 934 mAh g^{-1} was recovered. It is obvious that the capacity obtained at high rate is much higher than the bare Fe_3O_4 electrode and the recently reported value [27, 29-30, 32]. Excellent lithium storage performance is attributed to the unique sandwich structure, in which the graphene sheets are supposed to effectively accelerate electron transfer. The Fe_3O_4 nanoparticles connect with each other through the graphene sheets, resulting in the improvement of the electron transmission efficiency. What's more, the high surface area and hierarchical pore distribution are considered to be beneficial for fast ion transportation and short solid-state diffusion lengths, which are beneficial for high rate performance [39].

Electrochemical impedance spectroscopy (EIS) was conducted to further identify the electrode kinetic differences between the FGHF and bare Fe_3O_4 electrodes. As shown in Fig 5d, both samples exhibit similar Nyquist plots, delivering a depressed semicircle in the medium-frequency region and a linear tail in the low frequency region. The intercept on the real axis at the high-frequency end is the electrolyte resistance (Rs), the diameter of the semicircle at medium-frequency region gives charge-transfer resistance (Rct), and the inclined line in the low-frequency region represents the Warburg impedance (Zw) [27, 40, 41]. As shown in Fig 4d, the diameter of the semicircle for FGHF electrode in the highmedium-frequency region is significantly smaller than that of bare Fe_3O_4 electrode. Therefore, it can be assumed that the interparticle resistance and Rct of the Fe_3O_4-based electrode were reduced by hybridizing with graphene [41]. Lower Rct can lead to rapid electron transport and thus result in improved rate performance, which can well explain the better rate performance of the FGHF electrode [27].

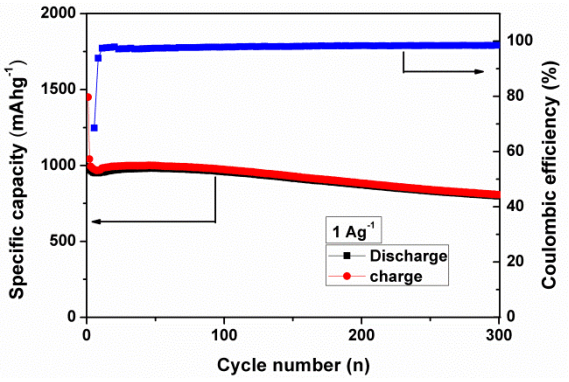

Figure 6. Cycling performance of the FGHF.

GCD cycle test was performed at 1 A g^{-1} to evaluate lithium storage stability. As shown in Fig. 6, the first charge and discharge capacities are 1451 and 994 $mAhg^{-1}$, respectively. After 300 cycles, the reversible capacity can be retained as 776 mA h g^{-1}, with a high capacity retention rate of 78%. As shown in Table 1, the FGHF provided excellent lithium storage performances compared with the recently reported similar anode materials. Such good cycle stability can be attributed to the structure advantages. The Fe_3O_4 nanoparticles are confined between graphene sheets, which greatly alleviate the volume effect and agglomeration of nanoparticles during the charging/discharging processes. As a result, improved cycle performances can be achieved.

Table 1 The lithium storage performances of recently reported similar anode materials.

Composites	Specific capacity/mAh g^{-1}	Current density/A g^{-1}	Cycle Numbers	Ref.
Fe_3O_4/graphene hybrid film	947	1	300	This paper
N-doped graphene/Fe_3O_4	1 227	3	1000	[1]
Fe_3O_4/C composites	803	0.4	300	[13]
Fe_3O_4-Fe@BCNT composite	785	0.5	300	[14]
Graphene foam/Fe_3O_4 anoparticles composite	1220	1	500	[15]
Fe_3O_4/C composite with hollow spheres in porous D-nanostructure	1300	0.1	100	[17]
Porous Fe3O4/carbon microspheres	746	1	300	[18]
Nanocomposite of rGO/Fe3O4/AC	835	1	300	[19]

The superiority of FGHF could be attributed to the following reasons. Firstly, this material combines the advantages both of graphene and Fe_3O_4, which is the typical feature of carbon-based materials. Namely, the graphene sheets are supposed to effectively accelerate electron transfer and endow the electrode with flexibility. While, Fe_3O_4 nanoparticles contribute to superior capacity. Secondly, the unique Sandwich structure plays a key role for the stronger stability. Thanks to the unique structure, the Fe_3O_4 nanoparticles are confined between graphene sheets, which greatly alleviate the volume effect and agglomeration of nanoparticles during the charging/discharging processes due to the buffer structure [2]. What's more, the Fe_3O_4 nanoparticles connect with each other through the graphene sheets, resulting in the improvement of the electron transmission efficiency.

Thirdly, the FGHF exhibited a high surface area and hierarchical pore distribution, which are very important for high-power LIBs [39].

4. CONCLUSION

In summary, Sandwich-structured Fe_3O_4/graphene hybrid film (FGHF) is successfully constructed by a facile strategy. Such a synthesis route endows FGHF integrated electrode with combined benefits of graphene sheets and Fe_3O_4 nanoparticles. The graphene sheets are supposed to effectively accelerate electron transfer and endow the electrode with flexibility. While, the Fe_3O_4 nanoparticles are confined between graphene sheets, which greatly alleviate the volume effect and agglomeration of nanoparticles during the charging/discharging processes due to the buffer structure. Therefore, the presented FGHF electrode exhibits excellent lithium storage performances..

ACKNOWLEDGMENTS
This work was supported by the National Natural Science Foundation of China (grant numbers U1504204, 21471135, 21506198).

References

1. W. Qi, X. Li, H. Li, W.K. Wu, P. Li, Y. Wu, C.J. Kuang, S.X. Zhou and X.L. Li, *Nano Res*., 10 (2017) 2923.
2. M. Li, H.R. Du, L. Kuai, K.F. Huang, Y.Y. Xia and B.Y. Geng, *Angew. Chem. Int. Edit*., 56 (2017) 12649.
3. J. Woods, N. Bhattarai, P. Chapagain, Y.H. Yang and S. Neupane, *Nano Energy*, 56 (2019) 619.
4. Y. Lu, L. Yu, X.W. Lou, *Nanostructured Conversion-type Anode Materials for Advanced Lithium-Ion Batteries, Chem,* 4 (2018) 972-996.
5. Z.G. Chen, Z.H. Hou, W.Y. Xu, Y.Y. Chen, Z. Li, L. Chen and W. Wang, *Electrochim. Acta*, 296 (2019) 206.
6. H. Yin, X.X. Yu, Q.W. Li, M.L. Cao, W. Zhang, H. Zhao and M.Q. Zhu, *J. Alloy. Compd*., 706 (2017) 97.
7. L.J. Wu, H. Li, X.M. Xie, K.K. Chai, P.L. Han, C. Zhang and C.C. Yang, *J. Alloy. Compd.,* 780 (2019) 482.
8. Y.F. Yuan, F. Chen, G.C. Cai, S.M. Yin, M. Zhu, L.N. Wang, J.L. Yang and S.Y. Guo, *Electrochim. Acta,* 296 (2019) 669.
9. K.W. Liu, F. Zou, Y.D. Sun, Z.T. Yu, X.Y. Liu, L.Y. Zhou, Y.F. Xia, B.D. Vogt and Y. Zhu, *J. Power Sources*, 395 (2018) 92.
10. S.P. Varghese, B. Babu, R. Prasannachandran, R. Antony and M.M. Shaijumon, *J. Alloy. Compd*., 780 (2019) 588.
11. S. Hwang, Q.P. Meng, P.F. Chen, K. Kisslinger, J.J. Cen, A. Orlov, Y.M. Zhu, E.A. Stach, Y.H. Chu and D. Su, *Angew. Chem. Int. Edit*., 56 (2017) 7813.
12. H.Y. Gu, Y.M. Zhang, M.Q. Huang, F. Chen, Z.H. Yang, X.M. Fan, S. Li, W.X. Zhang, S.H. Yang and M. Li, *Inorg. Chem*., 56 (2017) 7657.
13. C.G. Han, N. Sheng, C.Y. Zhu and T. Akiyama, *Mater. Today Energy*, 5 (2017) 187.
14. L.Y. Du, C.X. Xu, J.J. Liu, Y.Z. Lan and P.W. Chen, *Nanoscale*, 9 (2017) 14376.
15. Y. Huang, Z.H. Xu, J.Q. Mai, T.K. Lau, X.H. Lu, Y.J. Hsu, Y.S. Chen, A.C.H. Lee, Y.L. Hou, Y.S.

Meng and Q. Li, *Nano Energy*, 41 (2017) 426.
16. Y. Shi, J. Zhang, A.M. Bruck, Y.M. Zhang, J. Li, E.A. Stach, K.J. Takeuchi, A.C. Marschilok, E.S. Takeuchi and G.H. Yu, *Adv. Mater*., 29 (2017) 1603922.
17.]Z. Yang, D.Y. Su, J.P. Yang and J. Wang, *J. Power Sources*, 363 (2017) 161.
18. W.J. Han, X.Y. Qin, J.X. Wu, Q. Li, M. Liu, Y. Xia, H.D. Du, B.H. Li and F.Y. Kang, *Nano Res*., 11 (2018) 892.
19. R.R. Ding, J. Zhang, J. Qi, Z.H. Li, C.Y. Wang and M.M. Chen, *ACS Appl. Mater. Inter*., 10 (2018) 13470.
20. Y.S. Wang, Y.Y. Li, Z.P. Qiu, X.Z. Wu, P.F. Zhou, T. Zhou, J.P. Zhao, Z.C. Miao, J. Zhou and S.P. Zhuo, *J. Mater. Chem*. A, 6 (2018) 11189.
21. L.Y. Sun, L. Yang, J. Li, R.L. Narayan and X.H. Ning, , *Electrochim. Acta*, 288 (2018) 71.
22. C. Liao and S.P. Wu, , *Chem. Eng. J*., 355 (2019) 805.
23. Y.J. Duan, D.L. Zhao, X.H. Liu, H.X. Yang, W.J. Meng, M. Zhao, X.M. Tian and X.Y. Han, , *J. Alloy. Compd.,* 779 (2019) 466.
24. C. Liu, Q. Xia, C. Liao and S.P. Wu, *Mater. Today Commun*., 18 (2019) 66.
25. S. Hao, B. Zhang, Y. Wang, C. Li, J. Feng, S. Ball, M. Srinivasan, J. Wu and Y. Huang, *Electrochim. Acta,* 260 (2018) 965.
26. Z. Liu, X.-Y. Yu and U. Paik, *Adv. Energy Mater*., 6 (2016) 1502318.
27. C. He, S. Wu, N. Zhao, C. Shi, E. Liu and J. Li, *ACS Nano*, 7 (2013) 4459.
28. L. Li, A. Kovalchuk, H. Fei, Z. Peng, Y. Li, N.D. Kim, C. Xiang, Y. Yang, G. Ruan and J.M. Tour, *Adv. Energy Mater*., 5 (2015) 1500171.
29. Q. Zhao, J. Liu, Y. Wang, W. Tian, J. Liu, J. Zang, H. Ning, C. Yang and M. Wu, *Electrochim. Acta*, 262 (2018) 233.
30. Y.F. Mo, H.T. Zhang and Y.N. Guo, *Mater. Lett.,* 205 (2017) 118.
31. Y.T. Ma, J. Huang, X. Liu, F. Bu, L.S. Wang, Q.S. Xie and D.L. Peng, *Chem. Eng. J*., 327 (2017) 678.
32. Y. Suo, Q.Q. Zhao, J.K. Meng, J. Li, X.C. Zheng, X.X. Guan, Y.S. Liu and J.M. Zhang, *Mater. Lett.*, 174 (2016) 36.
33. J. Guo, H. Zhu, Y. Sun, L. Tang and X. Zhang, *Chem. Eng. J*., 309 (2017) 272.
34. Y. Liu, Y. Zhan, Y. Ying and X. Peng, *New J. Chem.,* 40 (2016) 2649.
35. J. Azadmanjiri, V.K. Srivastava, P. Kumar, M. Nikzad, J. Wang and A. Yu, *J. Mater. Chem*. A, 6 (2018) 702.
36. T. Yoon, J. Kim, J. Kim and J.K. Lee, *Energies*, 6 (2013) 4830.
37. W.S. Hummers and R.E. Offeman, *J. Am. Chem. Soc*., 80 (1958) 1339.
38. Y. Zhao, F. Wang, C. Wang, S. Wang, C. Wang, Z. Zhao, L. Duan, Y. Liu, Y. Wu, W. Li and D. Zhao, *Nano Energy*, 56 (2019) 426.
39. X.-Y. Yang, L.-H. Chen, Y. Li, J.C. Rooke, C. Sanchez and B.-L. Su, *Chem. Soc. Rev*., 46 (2017) 481.
40. J. Wang, J. Chen, K. Konstantinov, L. Zhao, S.H. Ng, G.X. Wang, Z.P. Guo and H.K. Liu, *Electrochim. Acta*, 51 (2006) 4634.
41. J.-Z. Wang, C. Zhong, D. Wexler, N.H. Idris, Z.-X. Wang, L.-Q. Chen and H.-K. Liu, *Chem. Eur*. J., 17 (2011) 661.